LATTICE BOLTZMANN DIRECT NUMERICAL SIMULATION OF TURBULENCE OVER RESOLVED AND MODELLED WALLS WITH IRREGULARLY DISTRIBUTED ROUGHNESS

Yusuke Kuwata,Yasuo Kawaguchi
Department of Mechanical engineering
Tokyo University of Science
2641 Yamazaki, Noda-city, Chiba, Japan
email a27900@rs.tus.ac.jp

ABSTRACT

To predict turbulence near rough walls without dealing with complicated roughness structures, a macroscopic rough wall model based on the volume averaging theory model is considered. The dispersive covariance and the drag force term, both of which need modelling, arise in the plane averaged momentum equation, however, the present model only models the drag force term which plays an important role inside the rough wall. Assuming that the drag force term can be considered as summation of the viscous and form drag force generated by each roughness element, it is analytically modelled with the plane porosity and the plane averaged hydraulic diameter. The direct and macroscopic model simulations are carried out by the D3Q27 multiple-relaxation time lattice Boltzmann method. It is found that the present model successfully predicts the increase of skin friction and the behaviour of the Reynolds stresses around the rough wall. It is found that since the influence of the dispersion on the momentum transport is marginal, the momentum transport around the rough wall can be reasonably reproduced by the macroscopic model. Furthermore, although the macroscopic model cannot directly solve the turbulence dissipation by the dispersive velocity fluctuation which is significant inside the rough wall, the drag force can reasonably compensate the unresolved dissipation.

BACKGROUND

In most geophysical and engineering flows, the underlying surface is usually rough. In the geophysical context, flows over vegetated, urban canopies and natural river beds can be classified to rough wall turbulence. Furthermore, rough surfaces usually occur in engineering devices due to imperfections in the production process, corrosions by aging, erosion or contamination. Those cause significant increase of turbulent frictional drag. Therefore, a large number of experimental studies have explored effective roughness parameters to predict the frictional drag. (e.g. Nikuradse1933; Moody1944; Flack et al., 2010) On the other hand, even though many direct numerical simulation (DNS) studies have been performed, fully resolving complicated rough wall geometry requires huge computational demands. One of the most effective approaches to reveal the underlying physics without huge computational demands is employing rough wall model (e.g., Orlendi et al., 2003; Scotti 2006; Bhanager 2008; Bussa and Sandham 2012). Busse and Sandham (2012) performed DNS of modelled rough wall by adding an extra force term in the Navier-Stokes equations. They reported that turbulent vortex structures and turbulent statistics over modelled rough wall showed similar trends to the previous experimental and numerical results. Orlendi et al., (2003) carried out DNS allowing the wall-normal velocity fluctuation at the wall and concluded that wall-normal velocity fluctuation was the driving parameter which leads to a drag increase. However, since their models were not based on the theoretical derivation and qualitatively evaluations were limited, their models did not reasonably mimic the rough wall. Hence, this research attempts to model the rough wall based on the volume averaging theory which has been usually applied to the porous medium flows (Whitaker 1986; Breugem et al., 2006; Kuwata and Suga 2016). Comparing the DNS results of turbulence over directly resolved and modelled rough walls, the validity of the rough wall model is investigated in detail. Furthermore, the underlying physics of rough wall turbulence is also discussed.

Numerical scheme

The present DNS is performed by the D3Q27 multiple relaxation time lattice Boltzmann method (MRT-LBM):

$$\begin{aligned} &\mid f(x+\xi_\alpha \delta t, t+\delta t)\rangle - \mid f(x,t)\rangle \\ &\qquad = -M^{-1}\hat{S}[\mid m(x,t)\rangle - \mid m^{eq}(x,t)\rangle] \\ &\qquad +M^{-1}\left(I-\tfrac{\hat{S}}{2}\right)M\mid F\rangle\delta t, \end{aligned} \tag{1}$$

where the notations such as $|\boldsymbol{f}\rangle$ is $|\boldsymbol{f}\rangle = (f_0, f_1, \cdots, f_{26})^T$, δt denotes the time step and ξ_α represents the discrete velocity. The matrix $\boldsymbol{M}$ is a 27×27 matrix which linearly transforms the distribution functions to the moments $|\boldsymbol{m}\rangle = \boldsymbol{M}|\boldsymbol{f}\rangle$. The collision matrix $\hat{\boldsymbol{S}}$ is diagonal;

$$\begin{aligned} &\hat{S} \equiv diag(0,0,0,0,s_4,s_5,s_5,s_7,s_7,s_7,s_{10},s_{10},s_{10},s_{13}, \\ &s_{13},s_{13},s_{16},s_{17},s_{18},s_{20},s_{20},s_{20},s_{23},s_{23},s_{23},s_{26}). \end{aligned} \tag{2}$$

The relaxation parameters are

$$\begin{aligned} &s_4 = 1.54,\ \ s_5 = s_7,\ \ s_{10} = 1.5,\ \ s_{13} = 1.83,\ \ s_{16} = 1.4, \\ &\qquad s_{17} = 1.61,\ \ s_{18} = s_{20} = 1.98,\ \ s_{23} = s_{26} = 1.74. \end{aligned} \tag{3}$$

The relaxation parameters s_5, s_7 are related to the kinematic viscosity ν,

$$\nu = c_s^2\left(\frac{1}{s_5}-\frac{1}{2}\right)\delta t = c_s^2\left(\frac{1}{s_7}-\frac{1}{2}\right)\delta t. \tag{4}$$

The equilibrium moments, transformation and collision matrixes presently employed are as in Suga et al. (2015). The term F is the external force term:

$$F_\alpha = w_\alpha \rho \left\{ \frac{\boldsymbol{\xi}_\alpha \cdot \boldsymbol{a}}{c_s^2} \left(1 + \frac{\boldsymbol{\xi}_\alpha \cdot \boldsymbol{u}}{c_s^2} \right) - \frac{\boldsymbol{a} \cdot \boldsymbol{u}}{c_s^2} \right\}, \tag{5}$$

where $\boldsymbol{a}$ is acceleration rate, $\boldsymbol{u}$ denotes the velocity vector, ρ is the fluid density and w_α is the weighting constant. The sound speed $c_s = 1/\sqrt{3}c$ with $c = \Delta/\delta t$ and Δ is the lattice spacing. The accuracy of the present method was confirmed to be equivalent to the spectrum method by Suga et al., (2015).

Macroscopic modelling of rough walls

To macroscopically solve flows inside rough walls, the $x-z$ plane averaging as illustrated in Figure 1 is applied to the governing equations. The definition of the superficial plane averaging of $\phi(x,y,z)$ is introduced as

$$\langle \phi(y) \rangle = \frac{1}{A_S} \int_S \phi(x,y,z) dS, \tag{6}$$

where S and A_S are the surface of the $x-z$ plane and the surface areas of S, respectively. A variable ϕ can be decomposed into the contribution from the intrinsic averaged value: $\langle \phi \rangle^f$ and deviation from the intrinsic averaged value: $\tilde{\phi}$ as

$$\phi = \langle \phi \rangle^f + \tilde{\phi}, \tag{7}$$

where the relation exists between the superficial and intrinsic plane averaged values as: $\langle \phi \rangle = \varphi \langle \phi \rangle^f$. The surface porosity φ is defined as $\varphi = A_S/A_{S_f}$. Here, A_{S_f} denotes the surface area of the fluid phase contained in S. Following Whitaker (1986), the plane averaged momentum equations for incompressible flows can be derived as

$$\begin{aligned} \frac{D\langle u_i \rangle^f}{Dt} = & -\frac{1}{\rho}\frac{\partial \langle p \rangle^f}{\partial x_i} + \frac{1}{\varphi}\frac{\partial}{\partial x_k}\left(\nu \frac{\partial \varphi \langle u_i \rangle^f}{\partial x_k} \right) - \frac{1}{\varphi}\frac{\partial}{\partial x_k} \varphi \langle \tilde{u}_i \tilde{u}_k \rangle^f \\ & \underbrace{- \frac{\nu}{\varphi}\frac{\partial \varphi}{\partial x_k}\frac{\partial \langle u_i \rangle^f}{\partial x_k}}_{g_i^\varphi} \underbrace{- \left(\frac{1}{\rho A_{S_f}} \int_S \tilde{p} n_i d\ell - \frac{\nu}{A_{S_f}} \int_S n_k \frac{\partial \tilde{u}_i}{\partial x_k} d\ell \right)}_{f_i}, \end{aligned} \tag{8}$$

where ℓ represents the length of the solid obstacle within an averaging surface and n_k is its unit normal vector pointing outward from the fluid to the solid phase. Since Breugem et al., (2006) reported that the covariant term $\langle \tilde{u}_i \tilde{u}_j \rangle^f$ was negligibly small, the present model does not model it. The term f_i is the drag force terms consisting of the surface integration of the dispersive viscous stress and the dispersive pressure.

When the surface porosity is nearly unity, the drag force term f_i in Eq.(8) can be assumed to be the arithmetical averaged force generated by each solid obstacle of diameter D_n:

$$\rho f_i \approx \frac{1}{A_{S_f}} \sum_{n=1}^{N} D_n C_D(n) \frac{\rho}{2} \langle \hat{u}_i \rangle^f \sqrt{\langle \hat{u}_k \rangle^f \langle \hat{u}_k \rangle^f}, \tag{9}$$

where N is the total number of obstacle in a certain $x-z$ plane, $\hat{u}$ is the relative velocity to the roughness: $\hat{u} = u - u_{rough}$, here u_{rough} is the moving velocity of the roughness. Considering the viscous and foam drag effects, the drag coefficient $C_D(n)$ can be modelled as

$$C_D(n) = \frac{C_1}{Re_D(n)} + C_2, \tag{10}$$

where C_1 and C_2 are the model constants. The Reynolds number: Re_{D_n} is defined as

$$Re_D(n) = D_n \sqrt{\langle \hat{u}_k \rangle^f \langle \hat{u}_k \rangle^f} / \nu. \tag{11}$$

Substituting Eqs. (10) and (11) in Eq. (9), the drag force can be written as

$$f_i = \nu \frac{C_1}{2} \frac{N}{A_{S_f}} \langle \hat{u}_i \rangle^f + \frac{C_2}{2} \langle \hat{u}_i \rangle^f \sqrt{\langle \hat{u}_k \rangle^f \langle \hat{u}_k \rangle^f} \frac{1}{A_{S_f}} \sum_{n=1}^{N} D_n. \tag{12}$$

Since the total number of obstacles N and the diameter D_n can not easily defined in complicated rough walls, some alternative parameters should be introduced. Accordingly, the present model considers the mean hydraulic (equivalent) diameter D_m defined as

$$\begin{aligned} D_m = \frac{4S_{sum}}{L_{sum}} &= \left(\frac{4}{N} \sum_{n=1}^{N} \frac{\pi D_n^2}{4} \right) / \left(\frac{1}{N} \sum_{n=1}^{N} \pi D_n \right) \\ &= (A_S - A_{S_f}) / \left(\sum_{n=1}^{N} D_n \right). \end{aligned} \tag{13}$$

where S_{sum} and L_{sum} are the total area occupied by obstacles S_{sum} and the total wetted perimeter of cylinders L_{sum}. Assuming the the total area occupied by obstacles: $A_S - A_{S_f}$ can be approximated as the product of the total number of obstacles and the mean hydraulic diameter:

$$N \frac{\pi}{4} D_m^2 \approx A_S - A_{S_f} = \left(\frac{1}{\varphi} - 1 \right) A_{S_f}, \tag{14}$$

With the help of Eqs.(14) and (13), the drag force term of Eq.(12) is further written as

$$f_i = \nu \frac{2C_1}{\pi} \frac{(1-\varphi)}{\varphi D_m^2} \langle \hat{u}_i \rangle^f + \frac{C_2}{2} \frac{(1-\varphi)}{\varphi D_m} \langle \hat{u}_i \rangle^f \sqrt{\langle \hat{u}_k \rangle^f \langle \hat{u}_k \rangle^f}. \tag{15}$$

It should be note that Eq.(16) is only valid when roughness distribution is sparse enough to neglect the mutual dependency of the drag force. When the roughness densely distributes namely $\varphi \approx 0$, we can deduce that the drag force behaves as that in packed beds. Considering limiting behaviour in such regions near $\varphi \to 0$, the multiplier of the surface porosity in a denominator of Eq.(16) is modified following the empirical equation of Ergun (1952) as

$$f_i = \nu \frac{2C_1}{\pi} \frac{(1-\varphi)}{\varphi^2 D_m^2} \langle \hat{u}_i \rangle^f + \frac{C_2}{2} \frac{(1-\varphi)}{\varphi D_m} \langle \hat{u}_i \rangle^f \sqrt{\langle \hat{u}_k \rangle^f \langle \hat{u}_k \rangle^f}. \tag{16}$$

The model constants $C_1 = 52.3$ and $C_2 = 1.2$ are presently used.

Results and Discussions

To evaluate the presently developed macroscopic rough wall model, this study performs DNS of turbulence over modelled and directly resolved rough-walled open channel

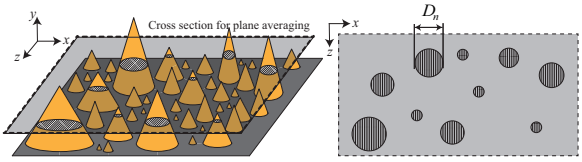

Figure 1. Sketch of the cross section for the plane averaging.

flows at the friction Reynolds number of 310. Figure 2 illustrates the computational geometry and the presently considered rough walls. The periodical boundary condition is applied to the steramwise and spanwise boundary faces with a constant streamwise pressure difference. A slip boundary is considered for the top boundary surface whilst the modelled or resolved rough wall is considered for the bottom wall. The presently employed rough walls consist of randomly packed semi-spheres. The semi-sphere diameters are given based on the Gaussian distribution and those semi-spheres are randomly packed at the bottom wall. To evaluate the model applicability, this study considers three rough walls of different equivalent roughness: k_s^+. The mean diameter μ is kept to be constant $\mu/\delta = 0.20$ whilst the standard deviation σ of the the Gaussian distribution is changed ($\sigma/\mu = 0.0, 0.17, 0.33$). The equivalent roughness estimated by the relation between the roughness function and k_+^s proposed by Nikuradse (1933) are $k_+^s = 21$, 42 and 92. The rough walls of $k_+^s = 21$, 42 and 92 are referred to KS21, KS42 and KS92, respectively. The PDF of surface height is shown in Figure 3 and the statistical moments of surface profiles are listed in Table1. Note that the value with the superscript "$()^+$" indicates the value normalised by the friction velocity of the rough wall. From Fig. 3, it is indicated the roughness elements of $h^+ \approx 30$ mostly occupies the rough wall in case KS21 whereas higher but sparser roughness elements exist in cases KS42 and KS92. This tendency is more remarkable in case KS92. The resolved wall simulation faithfully treats those rough walls with an interpolated bounce-back scheme which can impose the non-slip condition for curved boundaries whilst the model simulation applied volume averaged equation (Eq.(8)) with the drag force model in Eq.(16) to the rough wall region. Note that since the present roughness is stationary, the relative velocity $\hat{u}$ in Eq.(9) is the same as the fluid velocity u. The computational domain size is $6\delta(x) \times \delta(y) \times 3\delta(z)$. Both in the resolved and modelled rough wall simulations, the computational domain is decomposed into the finer and coarser resolution domains by the imbalance-correction zonal grid refinement method (Kuwata and Suga 2016) and the grid node numbers of finer and coarse domains are $1200(x) \times 70(y) \times 600(z)$ and $600(x) \times 66(y) \times 300(z)$, respectively. The resolution of finer and coarse grid regions is 1.56 and 3.13 wall units, respectively. Note that the grid resolution and the computational domain size are carefully examined by comparing the results with finer grid or larger domain simulation.

Figure 4 compares the instantaneous wall-normal vorticity fluctuation at the rough wall interface $y = y_{max}$. Both in the resolved and modelled simulation results, the streamwise elongated streaky structures can be observed in case KS21 whilst, in cases KS42 and KS92, the streaky structures become less organized and lose their strength. Although the vortex structure over the modelled wall is very similar to that over the resolved in cases KS21 and KS42,

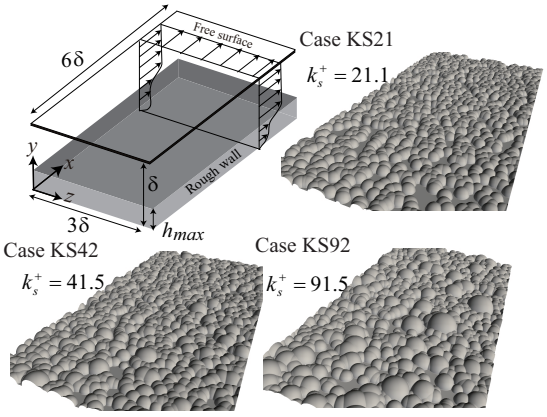

Figure 2. Computational geometry of rough-walled open channel flows.

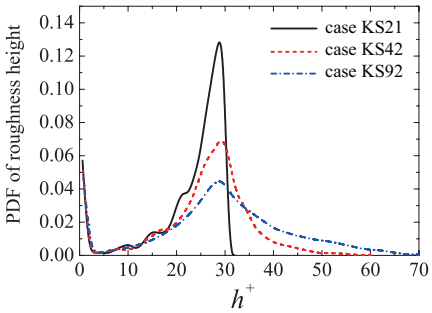

Figure 3. Probability density function of roughness height.

it can be observed that the streaky structures in case KS92 over the resolved wall are more shredded than that over the modelled wall. To discuss the intensity of the vorticity fluctuations, Figure 5 compares the $x-z$ planed averaged vorticity fluctuations intensities $\omega_{i,rms}$. It should be noticed that the vorticity $\boldsymbol{\omega} = \nabla \times \boldsymbol{u}$ inside the rough wall can be decomposed into the macro vorticity $\boldsymbol{\omega} = \nabla \times \langle \boldsymbol{u} \rangle^f$ and the micro vorticity (plane-dispersive vorticity) $\nabla \times \tilde{\boldsymbol{u}}$, however, since the present rough wall model solves the macroscopic flows, the micro-scale vorticity inside the rough wall is neglected. It is confirmed from Fig.5 that, although the pointed peak of $\omega_{y,rms}^+$ can be seen at the rough wall interface in case KS21, it loses strength in cases KS42 and KS92, which substantiates the vanishing of streaks as observed in Fig.4. Inside the rough wall, $\omega_{y,rms}^+$ rapidly decay in case KS21 whereas it reaches local maximum in cases KS42 and KS92. However, the local maximum value of $\omega_{y,rms}^+$ in cases KS42 and KS92 is far smaller than that in case KS21. Even though the above tendency can be captured by the modelled rough wall simulations, $\omega_{i,rms}^+$ is significantly underestimated inside the rough wall. This implies that the micro-scale vorticity is substantial inside the rough wall.

Figure 6 shows the superficial plane averaged streamwise mean velocity profiles. The DNS result of a smooth wall turbulent channel flow at $\mathrm{Re}_\tau = 300$ by **?** is also plotted for comparison. Because of the significant rise of wall friction, downward shift of the streamwise mean velocity profiles can be seen in all cases. As k_s^+ increases, the downward shift, which is referred as the roughness function, becomes more remarkable. It is confirmed that the increase of the roughness function is well captured by the modelled wall simulation and the agreement of the profiles with the

Table 1. Characteristics parameters of rough walls.

Case	h_m^+	h_{rms}^+	Sk	k_s^+	h_{max}/δ
KS21	22.3	7.95	-1.70	21.1	0.104
KS42	25.7	10.1	-0.73	41.5	0.185
KS92	30.0	14.5	0.21	91.5	0.285

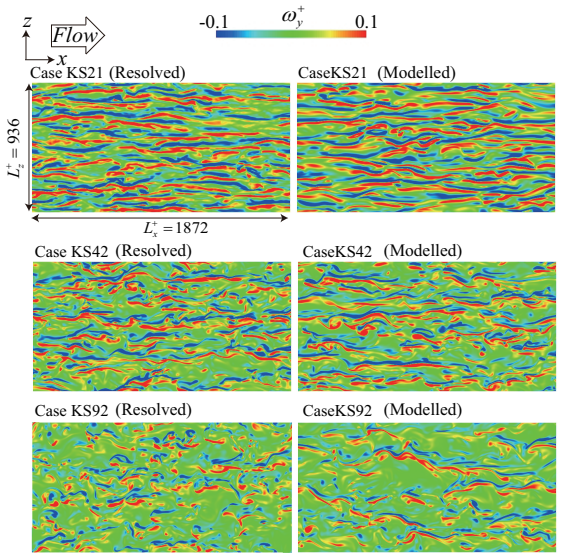

Figure 4. Instantaneous wall-normal vorticity fluctuation at the rough wall interface.

resolved wall simulation results is almost perfect.

Figure 7 compares the superficial plane averaged Reynolds normal stresses. Applying the volume averaging to the Reynolds stress, the volume averaged Reynolds stress: $R_{ij}^A = \langle \overline{u_i' u_j'} \rangle$ can be decomposed into the macro-scale Reynolds stress: $R_{ij} = \varphi \overline{\langle u_i' \rangle^f \langle u_j' \rangle^f}$ and the micro-scale (subfilter-scale) Reynolds stress: $r_{ij} = \varphi \langle \overline{\tilde{u}_i' \tilde{u}_j'} \rangle^f$. However, since the present model solves macroscopic flows and the micro-scale turbulence cannot be reproduced, the comparison is made between R_{ij}^A by the resolved wall simulations and R_{ij} by the modelled wall simulations. In Fig. 7, as k_s^+ increases, the Reynolds stresses are more damped by the wall roughness. The damping effect of the streamwise component is more remarkable than the other components. As k_s^+ increases, the location of the maximum of the streamwise component goes away from the wall and the maximum value becomes decrease. It is interesting to note that all profiles including the results over the smooth wall overlap at $y/\delta > 0.3$. This implies that the presence of the wall roughness does not affect the turbulence in the outer-layer, which substantiates the outer-layer similarity proposed by **?**. Although the micro-scale turbulence cannot be reproduced by the modelled wall simulation, the overall agreement of the Reynolds stress profiles with those by the resolved wall simulation is reasonable. However, inside the rough wall of case KS92, the model simulation slightly underpredicts the wall-normal and spanwise components. These results suggest that although the micro-scale turbulence is slightly produced inside the rough wall, the contribution to the momentum transport is not significant in the presently considered

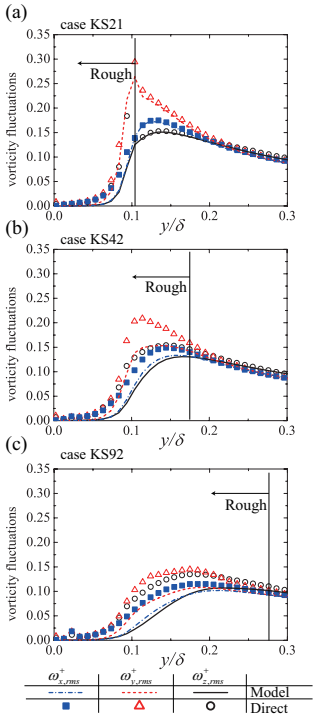

Figure 5. Intrinsic plane averaged vorticity intensities; (a) case KS21, (b) case KS42, (c) case KS92.

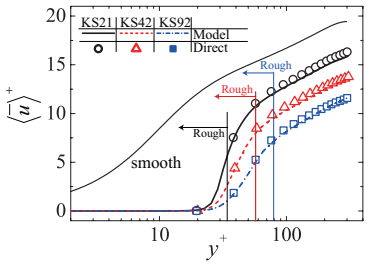

Figure 6. Intrinsic plane averaged streamwise mean velocity profiles.

rough walls of $k_s^+ < 90$ and the macroscopic model can reasonably predict those flows.

To discuss the momentum transport near the rough wall, x-z plane averaged momentum equations are discussed. Applying the integration of the momentum equation from 0 to y/δ, the momentum equation becomes

$$0 = -\frac{1}{\rho}\frac{\partial \langle \overline{p} \rangle^{f+}}{\partial x^*}\left(\int_0^1 \varphi dy^* - \int_0^{y^*} \varphi dy^*\right) + \underbrace{\frac{1}{Re_\tau}\frac{\partial \varphi \langle \overline{u} \rangle^{f+}}{\partial y^*}}_{VS}$$
$$\underbrace{-\varphi \langle \tilde{\tilde{u}}\, \tilde{\tilde{v}} \rangle^{f+}}_{DC} \underbrace{-\varphi \langle \overline{u'v'} \rangle^{f+}}_{RS} \underbrace{-\left(\int_0^{y^*} \varphi g_x^{\varphi+} dy^* - \int_0^1 \varphi g_x^{\varphi+} dy^*\right)}_{IC}$$
$$\underbrace{-\left(\int_0^{y^*} \varphi f_x^+ dy^* - \int_0^1 \varphi f_x^+ dy^*\right)}_{DF}, \qquad (17)$$

where the superscript $()^*$ denote the normalised distance by the boundary layer thickness: δ. The terms VS, DC, RS, IC and DF represent the viscous stress, plane dispersive covariance, Reynolds shea r stress, inhomogeneous correction and drag force terms, respectively. Figure 8 shows the budget terms of . In Fig.8(a), the viscous stress (VS) becomes significant near the rough wall interface in case KS21 and inflection point is located at the interface. In contrast, the

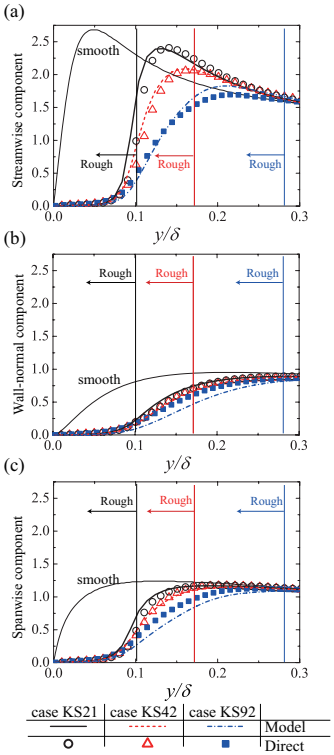

Figure 7. Intrinsic plane averaged Reynolds normal stresses; (a) streamwise component, (b) wall-normal component, (c) spanwise component.

VS profiles in cases KS42 and KS92 as shown in Fig.8(b) and (c) show peak inside the rough wall and the maximum value is smaller than that in case KS21. Inside the rough wall, the Reynolds stress (RS) decays to zero whilst the drag force (DF) and inhomogeneous correction (IC) terms substantially contribute. As k_s^+ increases, the contribution of VS and IC inside the rough wall considerably decreases whilst the drag force contribution increases. In case K92 as shown in Fig.8(c), the DF gradually works inside rough wall and the damping of the RS is also gradual. It is found that the plane dispersive covariant (DC) term is negligibly small in cases KS21 and KS42 whereas its contribution becomes meaningful in case KS92 near $y/\delta = 0.15$. Through the comparison the results between resolved and modelled simulations, even though the macroscopic model drops the DC, the reasonable agreement with the budget terms of the resolved simulation can be seen. However, inside the rough wall in case KS92, it is found that the RS contribution is underpredicted whilst the DF contribution is overpredicted. To discuss the turbulent transport, the transport equation of the macro-scale turbulent kinetic energy: $k = R_{kk}/2$ and the volume averaged turbulent kinetic energy: $k^A = R^A_{kk}/2$ are considered for the modelled and resolved wall simulations, respectively. The transport equation of k can be derived as

$$\frac{Dk}{Dt} = \underbrace{-\frac{\partial}{\partial x_k}\left(\frac{\varphi}{2}\overline{\langle u_i'\rangle^f\langle u_i'\rangle^f\langle u_k'\rangle^f}\right)}_{D_k^t} \underbrace{-\frac{\partial}{\partial x_k}\left(\varphi\frac{\overline{\langle u_k'\rangle^f\langle p'\rangle^f}}{\rho}\right)}_{D_k^p}$$
$$\underbrace{+\frac{\partial}{\partial x_k}\left(\varphi\nu\frac{\partial k}{\partial x_k}\right)}_{D_k^\nu} \underbrace{+2\nu k\frac{\partial^2\varphi}{\partial x_k^2}}_{G_k^\varphi} \underbrace{-\varphi\overline{\langle u_i'\rangle^f\langle u_k'\rangle^f}\frac{\partial\langle\overline{u_i}\rangle^f}{\partial x_k}}_{P_k}$$
$$\underbrace{-\varphi\nu\overline{\frac{\partial\langle u_i'\rangle^f}{\partial x_k}\frac{\partial\langle u_i'\rangle^f}{\partial x_k}}}_{\varepsilon_k} \underbrace{-\varphi\overline{f_i'\langle u_i'\rangle^f}}_{F_k}, \qquad (18)$$

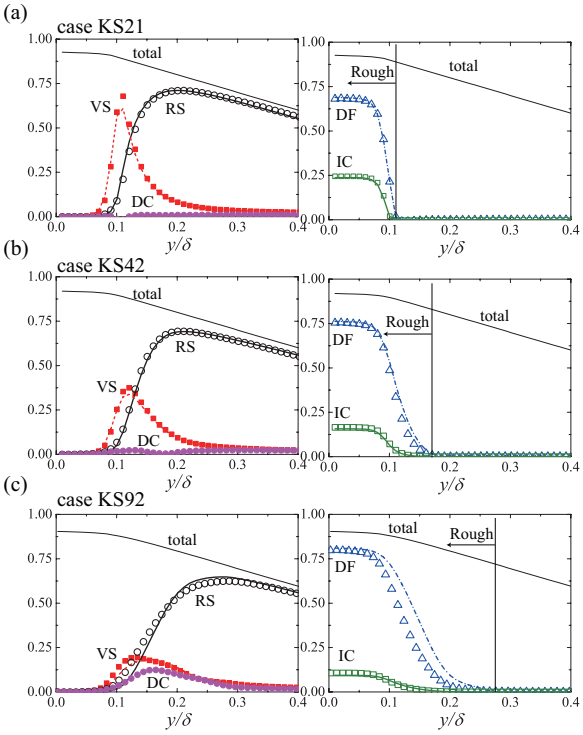

Figure 8. Budget terms in the plane averaged momentum equations; (a) case KS21, (b) case KS42, (c) case KS92; symbols: direct simulation, lines: model simulation.

where D_k^t, D_k^p, D_k^ν, G_k^φ, P_k, ε_k and F_k are the turbulent diffusion, pressure diffusion, viscous diffusion, inhomogeneous correction, production, dissipation and drag force terms for the macro-scale turbulent kinetic energy, respectively.

The transport equation of k^A can be derived as

$$\frac{Dk^A}{Dt} = \underbrace{-\frac{\partial}{\partial x_k}\left(\frac{\varphi}{2}\overline{\langle u_i'u_i'u_k'\rangle^f}\right)}_{D_{k^A}^t} \underbrace{-\frac{\partial}{\partial x_k}\left(\varphi\frac{\overline{\langle u_k'p'\rangle^f}}{\rho}\right)}_{D_{k^A}^p}$$
$$\underbrace{+\frac{\partial}{\partial x_k}\left\langle\varphi\nu\frac{\partial\frac{1}{2}\overline{u_i'u_i'}}{\partial x_k}\right\rangle^f}_{D_{k^A}^\nu} \underbrace{-\frac{\partial}{\partial x_k}\varphi\left\langle\tilde{\bar{u}}_k\overline{u_i'u_i'}\right\rangle^f}_{D_{k^A}^{\mathscr{T}}}$$
$$\underbrace{-\varphi\left\langle\overline{u_i'u_k'}\frac{\partial\overline{u_i}}{\partial x_k}\right\rangle^f}_{P_{k^A}} \underbrace{-\varphi\left\langle\nu\overline{\frac{\partial u_i'}{\partial x_k}\frac{\partial u_i'}{\partial x_k}}\right\rangle^f}_{\varepsilon_{k^A}}, \qquad (19)$$

where $D_{k^A}^t$, $D_{k^A}^p$, $D_{k^A}^\nu$, $D_{k^A}^{\mathscr{T}}$, P_{k^A} and ε_{k^A} are the turbulent diffusion, pressure diffusion, viscous diffusion, dispersion transport, production and dissipation terms for the volume averaged turbulent kinetic energy, respectively. Figure 9 presents the production, dissipation, turbulent diffusion, pressure diffusion and viscous diffusion terms. Note that since the contribution of the terms G_k^φ and $D_{k^A}^{\mathscr{T}}$ are confirmed to be negligibly small, they are not plotted in Fig. 9. In case KS21 shown in Fig.9 (a), the production become maximum over the rough wall and rapidly decay to zero inside the rough wall at $y/\delta = 0.75$. Although the modelled simulation does not take account of the micro-scale turbulence (dispersion fluctuation), the production, turbulent, pressure and viscous diffusion terms in the modelled simulation agree well with those in the resolved simulation whilst the dissipation ε in the modelled simulation is far smaller than ε^A. This implies that the micro-scale turbu-

lence hardly contributes to the turbulence generation and diffusion processes inside the rough wall, however, it plays a significantly important role in the turbulent dissipation. However, interestingly, it is found that sum of the dissipation ε and the drag force F_k by the modelled simulation agrees well with ε^A. The role of F_k in turbulence transport was discussed by Kuwata and Suga (2016) and they stated that, in the volume and Reynolds averaged system, the drag force term in Eq.(18) played an role of the energy transfer from the macro-scale turbulence to the micro-scale turbulence. The present result of $F_k \approx \varepsilon^A - \varepsilon$ implies that micro-scale turbulence production is mostly due to the energy transfer from the macro-scale turbulence and the micro-scale turbulence reaches the local equilibrium state: $F_k \approx \varepsilon^A - \varepsilon$. This also implies that the turbulent dissipation by the micro-scale turbulence can be reasonably modelled by F_k. In Figure 9 (a) (b) and (c), as k_s^+ increases, all budget terms decrease inside the rough wall, however, the levels of the production and dissipation terms at $y/\delta = 0.3$ in all cases remains unchanged. Furthermore, the turbulent production reaches maximum over the rough wall in case KS21, the location of the maximum shifts inside the rough wall in cases KS42 and KS92. Although the above tendency is well captured by the modelled simulation, inside the rough wall in case KS92 of $y/\delta < 0.15$, P^k and ε by the modelled simulation are smaller than P_k^A and ε^A, respectively. This indicates that the influence of the dispersion cannot be negligible inside the rough wall in case KS92, however, the influence of the dispersion is limited inside the rough wall.

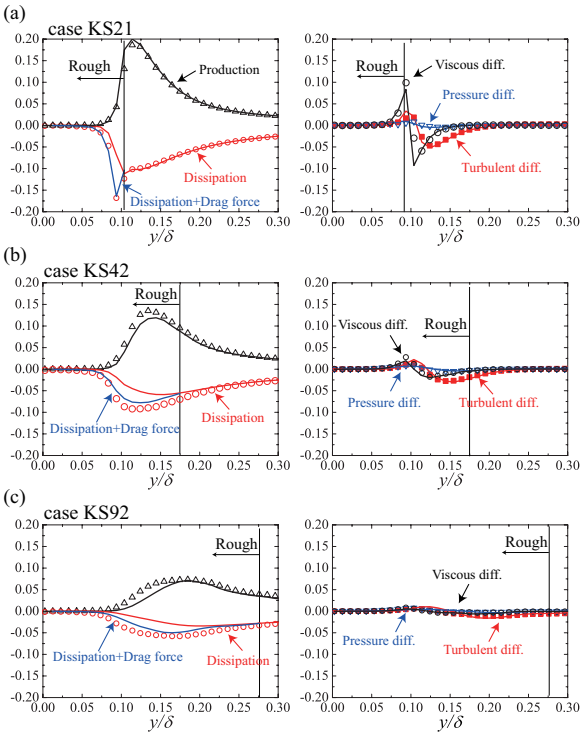

Figure 9. Budget terms in the transport equation of the intrinsic plane averaged turbulent kinetic equations; (a) case KS21, (b) case KS42, (c) case KS92; symbols: direct simulation, lines: model simulation.

1 Conclusion

To predict turbulence over rough walls without resolving complicated wall roughness, macroscopic rough wall model is developed. Assuming that the drag force term, which arises through the plane averaging of the Navier-Stokes equation, can be considered as summation of the viscous and form drag force generated by each roughness element, it is analytically modelled with the surface porosity and the hydraulic diameter. The direct and macroscopic model simulations for turbulence over irregularly distributed semi-spheres at the friction Reynolds number of 310 are carried out by the D3Q27 multiple-relaxation time lattice Boltzmann method. It is found that the present model successfully predicts the increase of skin friction and the behaviour of the Reynolds stress profiles around the rough wall is well predicted. Furthermore, it is found that since the influence of the dispersion on the momentum transport is marginal, the momentum transport around the rough wall can be reasonably reproduced even by the macroscopic model. Although the macroscopic model cannot directly solve the turbulence dissipation by the dispersive velocity fluctuation which is significant inside the rough wall, the drag force can reasonably compensate that unresolved dissipation. Townsend (1980)

REFERENCES

Bhaganagar, Kiran 2008 Direct numerical simulation of unsteady flow in channel with rough walls. *Phys. Fluids* **20** (10), 101508.

Breugem, WP, Boersma, BJ & Uittenbogaard, RE 2006 The influence of wall permeability on turbulent channel flow. *J.urnal of Fluid Mechanics* **562**, 35–72.

Busse, A & Sandham, ND 2012 Parametric forcing approach to rough-wall turbulent channel flow. *Journal of Fluid Mechanics* **712**, 169–202.

Ergun, Sabri 1952 Fluid flow through packed columns. *Chem. Eng. Prog.* **48**, 89–94.

Flack, Karen A & Schultz, Michael P 2010 Review of hydraulic roughness scales in the fully rough regime. *J. Fluids Engrg.* **132** (4), 041203.

Kuwata, Y & Suga, K 2016*a* Imbalance-correction grid-refinement method for lattice boltzmann flow simulations. *Journal of Computational Physics* **311**, 348–362.

Kuwata, Yusuke & Suga, Kazuhiko 2016*b* Transport mechanism of interface turbulence over porous and rough walls. *Flow, Turb. Combust.* **97** (4), 1071–1093.

Moody, Lewis F 1944 Friction factors for pipe flow. *Trans. Asme* **66** (8), 671–684.

Nikuradse, Johann 1933 Laws of flow in rough pipes .

Orlandi, P, Leonardi, S, Tuzi, R & Antonia, RA 2003 Direct numerical simulation of turbulent channel flow with wall velocity disturbances. *Physics of Fluids (1994-present)* **15** (12), 3587–3601.

Scotti, A 2006 Direct numerical simulation of turbulent channel flows with boundary roughened with virtual sandpaper. *Physics of Fluids* **18** (3), 031701.

Suga, K, Kuwata, Y, Takashima, K & Chikasue, R 2015 A d3q27 multiple-relaxation-time lattice boltzmann method for turbulent flows. *Computers & Mathematics with Applications* **69** (6), 518–529.

Townsend, Albert A 1980 *The structure of turbulent shear flow*. Cambridge university press.

Whitaker, S 1986 Flow in porous media i: A theoretical derivation of darcy's law. *Transport in porous media* **1** (1), 3–25.